JACS
JOURNAL OF THE AMERICAN CHEMICAL SOCIETY
pubs.acs.org/JACS
Article

A Comprehensive Landscape for Fibril Association Behaviors Encoded Synergistically by Saccharides and Peptides

Rongying Liu, Ran Zhang, Long Li, Zdravko Kochovski, Lintong Yao, Mu-Ping Nieh, Yan Lu, Tongfei Shi, and Guosong Chen*

Cite This: *J. Am. Chem. Soc.* 2021, 143, 6622−6633

Read Online

ACCESS | Metrics & More | Article Recommendations | Supporting Information

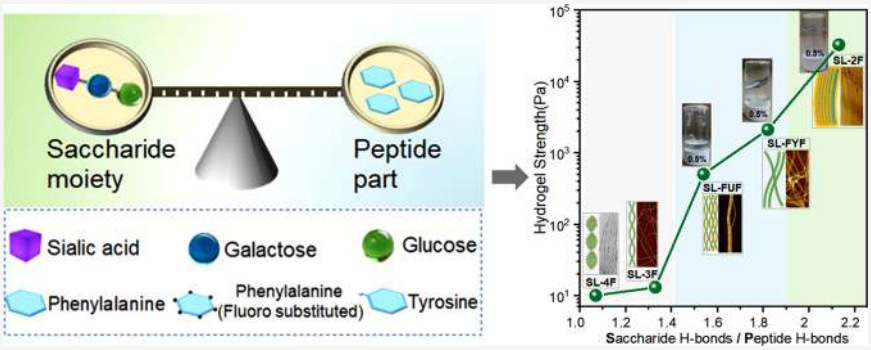

ABSTRACT: Nature provides us a panorama of fibrils with tremendous structural polymorphism from molecular building blocks to hierarchical association behaviors. Despite recent achievements in creating artificial systems with individual building blocks through self-assembly, molecularly encoding the relationship from model building blocks to fibril association, resulting in controlled macroscopic properties, has remained an elusive goal. In this paper, by employing a designed set of glycopeptide building blocks and combining experimental and computational tools, we report a library of controlled fibril polymorphism with elucidation from molecular packing to fibril association and the related macroscopic properties. The growth of the fibril either axially or radially with right- or left-handed twisting is determined by the subtle trade-off of oligosaccharide and oligopeptide components. Meanwhile, visible evidence for the association process of double-strand fibrils has been experimentally and theoretically proposed. Finally the fibril polymorphs demonstrated significant different macroscopic properties on hydrogel formation and cellular migration control.

Downloaded via FUDAN UNIV on May 11, 2021 at 06:49:23 (UTC).
See https://pubs.acs.org/sharingguidelines for options on how to legitimately share published articles.

■ INTRODUCTION

Fibril associations are ubiquitous in key life processes, e.g., actin filaments cross-linking into actin bundles,[1] collagen fibers hierarchically associating into soft tissues,[2] and amyloid fibrils pathologically associating into amyloid plaque,[3] to name a few. The knowledge of the underlying mechanism of fibril association is the foundation of understanding diverse key life processes. Meanwhile, fibril associations also dictate chirality,[4] optical characteristics,[5,6] and mechanical properties of fibrous materials.[7−9] Thus, the rationale of fibril association is vitally important for the design and development of fibrous materials.

Studies devoted to the fibril association have been emergent. The phenomenon began to be understood by using statistical analysis of atomic force images from the viewpoint of polymer physics.[10] Recently, some associated fibril species such as bundles of intertwined fibers[11] and braided fibrils[12] have been achieved based on some individual amphiphilic models that are far from their natural blueprints in structural aspects. Despite these cases having successfully provided a glimpse of fibril association,[13,14] a comprehensive picture of the fibril association behaviors starting from the molecular level of building blocks has not yet been targeted. A comprehensive landscape from molecular design to fibril structure and then fibril association behaviors, resulting in controllable material property, would greatly enhance our ability to design functional fibrous materials.

Given the glycoprotein/proteoglycan nature of some fiber-forming proteins such as collagen,[15] α-synuclein,[16] and fibronectin,[17] more importantly, both the saccharide moiety and peptide part appear to be involved in fibril association of glycoproteins with elusive explanations.[15] For example, *O*-GlcNAcylation was found to be able to alter the aggregation of α-synuclein.[18−20] It appears more rational to leverage glycopeptide models to perform fibril association research

Received: February 25, 2021
Published: April 26, 2021

© 2021 American Chemical Society

https://doi.org/10.1021/jacs.1c01951
J. Am. Chem. Soc. 2021, 143, 6622−6633

than use simple short peptide models. Despite significant achievements in creating artificial one-dimensional structures through self-assembly of short peptides,[21−24] the synergic effect of saccharides and peptides within this landscape of fibril association remains elusive.

Here, we provide a family of glycopeptide models with oligosaccharide and oligopeptide components. Both of the components have a significant structural contribution to fibril formation and the subsequent association. By controlling the subtle balance of the hydrogen bonds between oligosaccharides and those between oligopeptides as well as other interactions, a library of typical fibril association behaviors has been exhibited, such as single protofibrils laterally associated into flat multistrand ribbons, laterally associated into twisted left-handed double-strand fibrils, or radially associated into twisted right-handed nanoribbons. By combining experimental evidence and results from all-atom dynamics simulation, the whole process from fibril formation to association and related properties has been well elucidated by the competition between strand-forming and strand-association, the competition between the hydrogen bonds from oligosaccharides or oligopeptides, and a set of antagonistic interactions between electrostatic repulsion and hydrophobic interaction. In addition, visible evidence for the association process of double-strand fibrils has been experimentally and theoretically proposed. The links between fibril association behavior and some macroscopic properties such as hydrogelation and cell−matrix interaction have also been identified. In short, the present work would shed light on breaking the molecular code governing fibril association and would open up tremendous opportunities for the design of fibrous materials.

■ RESULTS AND DISCUSSION

Selection and Fabrication of Models for Fibril Association. To achieve a comprehensive landscape of fibril association behaviors, a set of glycopeptide models with the possibility of associating into different fibrils is required. In the literature, short peptides have been employed as model compounds to prepare various fibrils, in which the peptide moieties either preferably adopt antiparallel packing manner[25,26] or occasionally adopt a parallel packing manner.[27] Due to the lack of another component that can reasonably check and balance peptide component, these unbalanced peptidic models with the propensity to adopt antiparallel packing manner seems to be difficult to map a comprehensive landscape of fibril association behaviors. To some extent, it could be that although fibrils based on short peptides have been widely investigated, the related fibril association behavior has not been understood at the molecular level.

To solve this problem, we sought to construct a balanced glycopeptide model with a propensity to adopt a parallel packing manner, instead of antiparallel packing, in the fibril of the glycopeptide. For this type of balanced glycopeptide model, the interactions between saccharides should be compatible with the interactions between peptides. Meanwhile, the spatial size of the two parts should be compatible too. To access this type of glycopeptide model, triphenylalanine (denoted as **3F**) was first selected as the peptide moiety concerning its proven potential for fibril formation.[28] To seek a saccharide part that could match triphenylalanine in terms of interactions and spatial size and thus afford a parallel packing model, we screened some typical oligosaccharides such as lactose (**Lac**), trimannose (**TMan**), maltotriose (**MalT**), and sialyllactose (**SL**) by molecular simulation after considering the complexity and availability of saccharides. It was observed that the protofilament (starting structure) formed by the glycopeptide model of **SL-3F** (Scheme 1 a, 1b) in a parallel

Scheme 1. (a, b) Representative Model of SL-3F, All-Atom Molecular Dynamics Simulation Results for (c) Antiparallel Packing Mode and (d) Parallel Packing Mode, Quantified Comparison of Hydrogen Bonds Formed by (e) Saccharide Part (Saccharide H-Bonds), and (f) Two Components (Saccharide Part and Peptide Moiety) (Total H-Bonds) in Parallel Packing Mode and Antiparallel Packing Mode (12 × SL-3F)

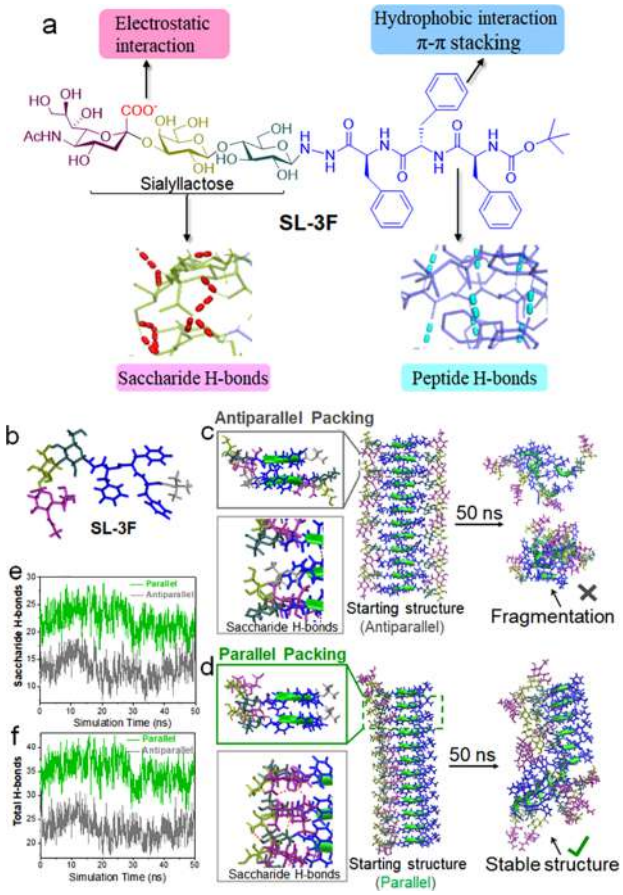

manner still remained stable after 50 ns relaxation but the counterpart in an antiparallel manner tended to fragment (Scheme 1c,d), whereas other glycopeptide models such as **Lac-3F**, **TMan-3F**, and **MalT-3F** seemingly could not well match triphenylalanine to afford a stable protofilament after the same relaxation time (Schemes S1−S3). The outcome suggested that the sialyllactose, a trisaccharide with a terminal negative charge and an extended conformation (Scheme 1a) appeared to be capable of matching triphenylalanine so as to afford a desired glycopeptide model that preferably adopted parallel packing as confirmed by the outperformance of parallel packing to antiparallel packing in terms of saccharide H-bonds and total H-bonds (Scheme 1e,f, Scheme S4).

SL-3F Associates into Twisted Double-Strand Fibrils. **SL-3F** was synthesized via a coupling reaction between the hydrazide group of triphenylalanine and the reducing end of the sialyllactose (for details, see Schemes S5 and S6). Then the compound was dispersed in water at 1 mg/mL. After several

https://doi.org/10.1021/jacs.1c01951
J. Am. Chem. Soc. 2021, 143, 6622−6633

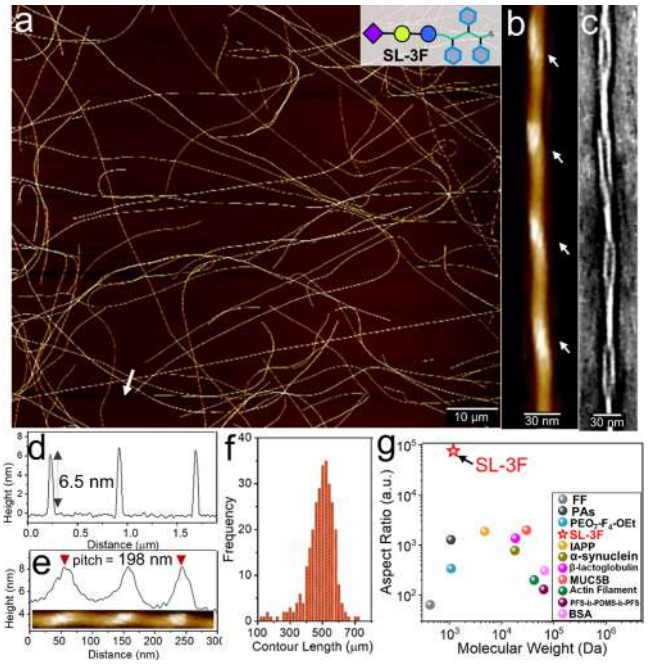

Figure 1. Fibril association behavior of **SL-3F** (1 mg/mL of **SL-3F** in water). (a, b, d, e) AFM height images and corresponding profiles of double-strand fibrils, (c) negatively stained TEM image, (f) statistical result of contour length of **SL-3F**, (g) a diagram showing aspect ratio versus molecular weight of building blocks for various fibrous assemblies (details in Table S1).

days, a fibrous structure was found in the solution. The combination of transmission electron microscopy (TEM), cryo-electron microscopy (cryo-EM), and atomic force microscopy (AFM) proved that **SL-3F** gave rise to well-defined fibrous structures (Figure 1a−c, Figure S1). These resultant fibrous species were found to be left-handed and double-stranded (Figure 1b,c), which was further evidenced by electron tomography (Figure S2). These double-strand fibrils appeared to be uniform with respect to diameter (∼6.5 nm) and pitch (∼198 nm) (Figure 1d,e). Very interestingly, these double-strand fibrils have contour lengths up to hundreds of microns (Figure 1f) yet seem to be capable of highly surviving in solution after even 1 year of incubation as confirmed by the unobservable slope variation in small-angle X-ray scattering (SAXS) data (Figure S3a). The aspect ratio of these fibrils is as high as 10^5 (Figure 1g), which seems larger than that of fibrous populations built by synthetic small molecules even naturally occurring biomacromolecules (Table S1). This extra-high aspect ratio reveals the great stability of **SL-3F** building blocks in the double strand fibrils, indicating our successful initiation of designing **SL-3F**.

To understand the fibril association behavior, the formation process of the double-strand fibrils was traced by means of TEM and AFM (Figure 2). It revealed that micelles initially formed (Figure 2a) then further fused into protofilaments (Figure 2b), which would grow into single-strand protofibrils (Figure 2c) with heights of 3.2 nm. Interestingly, these single-strand protofibrils tended to laterally associate into ribbon-like structure (as marked in Figure 2c), indicating their high propensity with respect to lateral association. After 12 h incubation, some single-strand protofibrils within ribbon-like structures were found to associate into double-strand fibrils as confirmed by the emergence of fibrous species with a height of 6.5 nm (Figure 2d, marked with red arrows). The remaining single-strand protofibrils tended to complete the double-strand process within 12 d once a small amount of double-strand fibrils formed (Figure 2e−g). Cryo-EM, SAXS, circular dichroism (CD), and UV−vis spectra were also used to confirm the association processes of **SL-3F** mentioned above (Figure S4−S6). The fibril association behaviors here reported, namely, a single-strand protofibril initially formed and then laterally associated into a ribbon-like structure where two single-strand protofibrils intertwined into double-strand fibrils

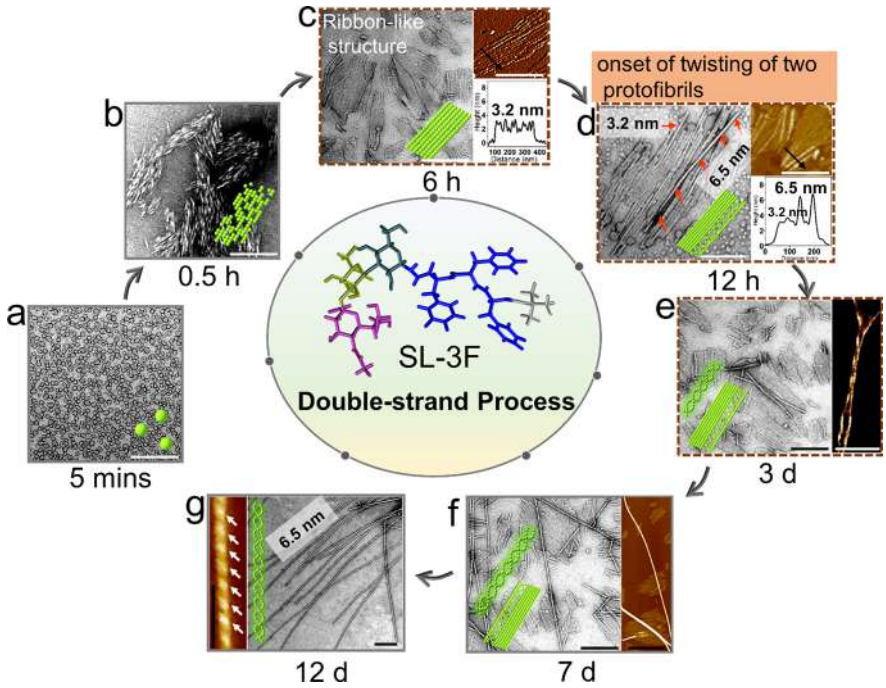

Figure 2. Association processes of **SL-3F** as a function of incubation time; all scale bars are 50 nm (1 mg/mL of **SL-3F** in water).

https://doi.org/10.1021/jacs.1c01951
J. Am. Chem. Soc. 2021, 143, 6622−6633

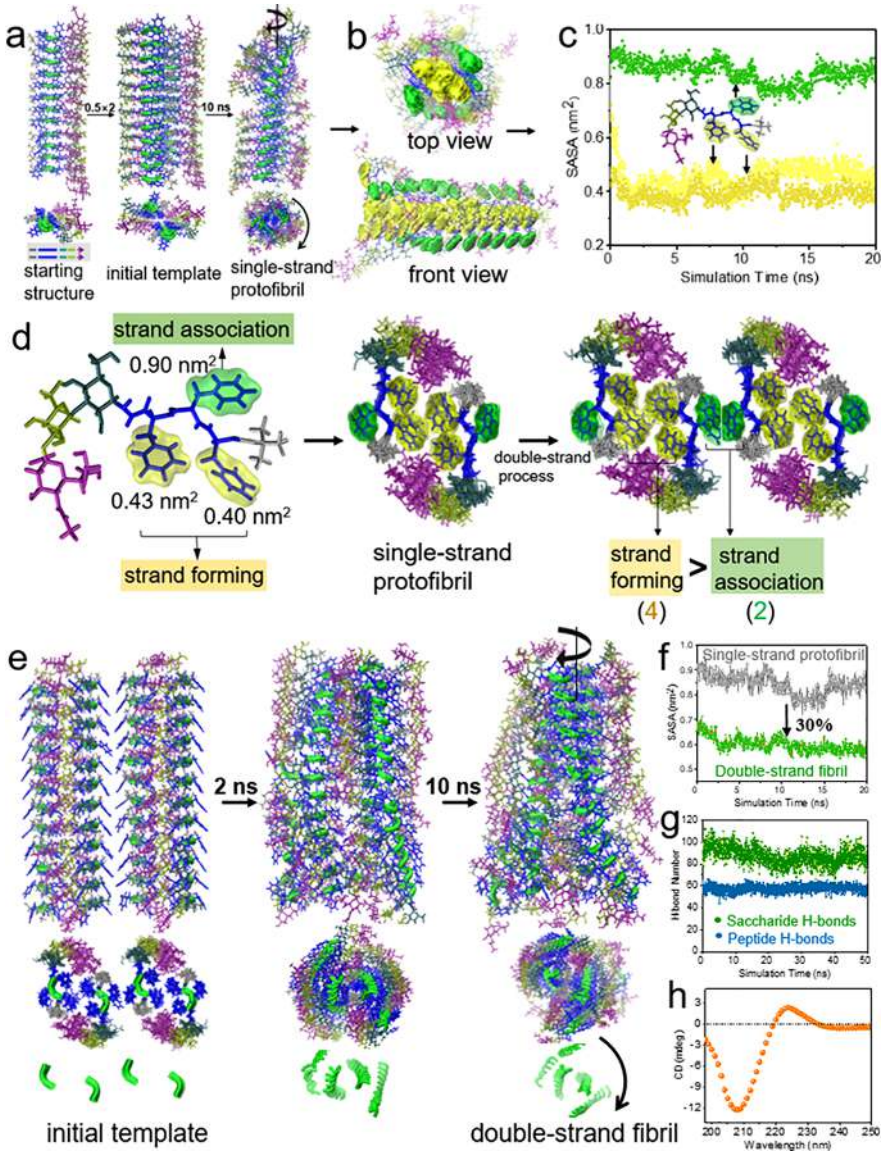

Figure 3. All-atom simulation for double-strand process. (a) relaxation process of **SL-3F** single-strand protofibril adopting parallel packing mode. (b) Top view and front view of single-strand protofibril of **SL-3F** after blurring of the saccharide moiety. (c) Average statistical results of solvent-accessible surface area (SASA) of each phenylalanine residue of **SL-3F**, (d) illustration for the competition between strand-forming and strand-association. (e) Relaxation process of double-strand fibril of **SL-3F**. (f) SASA value of the phenylalanine residue contributed to strand association before and after undergoing the double-strand process, (g) the statistical results of two types of H-bonds involved in double-strand fibrils of **SL-3F**, (h) CD result of double-strand fibrils of **SL-3F** (1 mg/mL, water).

after a long induction period (Figure 2d), may provide the first visible evidence of double-stranded process of fibrils.

To rationalize this double-stranded process, molecular dynamics simulation was performed to afford the detail at an atomic level. As mentioned above, a starting structure in a parallel manner (Figure 3a, left) was defined (details in Figure S7), yet this amphiphilic structure may tend to form the initial template of single-strand protofibril in a way that the two hydrophobic ends of **SL-3F** close together (Figure 3a, middle) to reduce the exposure of hydrophobic end to water. After 10 ns simulation, a stable single-strand protofibril with remarkable left-handed feature emerged (Figure 3a, right).

Next, we attempted to rationalize the association of single-strand protofibril into double-stranded fibril. After blurring the saccharide moiety on the surface of a balanced single-strand protofibril, it was readily found that most phenylalanine residues tended to be embedded in the protofibril (marked as yellow in Figure 3b), while a small amount of phenylalanine residues (marked as green in Figure 3b) were still prone to expose on the surface. The calculation of solvent accessible surface area (SASA) allowed us to quantitatively identify the role of each phenylalanine residue of a **SL-3F** molecule (Figure 3c). The SASA value of the middle phenylalanine residue (in green in Figure 3d) was determined to be 0.90 nm^2, but this value for the two phenylalanine residues at both sides (in yellow in Figure 3d) was only 0.43 and 0.40 nm^2. This quantified result clearly suggested that the two phenylalanine residues at both sides that tended to be buried in the protofibril would contribute to strand formation, while the middle phenylalanine residue that was prone to expose on the protofibril surface was most likely involved in strand association (Figure 3d). Thereby four hydrophobic phenyl-

https://doi.org/10.1021/jacs.1c01951
J. Am. Chem. Soc. 2021, 143, 6622−6633

alanine residues appeared to engage in strand formation, but only two hydrophobic phenylalanine residues would drive single-strand protofibrils to laterally associate (Figure 3d). That is, the driving force for strand formation seemed to be larger than that for strand-association; in this case, strand formation appeared to be preferred, accounting for the high restraint of this type of protofibril with respect to lateral association.

Based the single-strand protofibril model, the formation of a double-strand fibril was simulated starting from two laterally located single-strand protofibrils, as indicated from our AFM observation (Figure 2c,d). It was found that a stable double-strand fibril structure with striking left-handed tendency was yielded after a 10 ns relaxation on the initial template of double-strand fibril (Figure 3e, supporting movie 1). The simulation results showed that the average SASA of the middle phenylalanine responsible for strand-association decreased from 0.90 nm^2 for a single-strand protofibril to 0.59 nm^2 for a double-strand fibril (Figure 3f), implying that the potential of further lateral association of single-strand protofibril was attenuated significantly by double-stranded association. In addition, the all-atom simulation further suggested that only double-strand fibrils came to emerge after certain relaxation time even if more than two single-strand protofibrils constituted the initial template (Figure S8). This result was consistent with the aforementioned discussion, where the driving force for strand-forming exceeded that for strand-association and the single-strand protofibril preferentially associated into double-strand species rather than underwent infinite lateral association.

In short, the all-atom simulation explained the fibril association very well since the obtained simulation structure of the single-stranded protofibrils and double-stranded fibrils were quite consistent with the experimental results. The diameter of the single-strand protofibril of the simulation model can be measured as 3.2 nm (Figure S9a), which is consistent to the diameter measured by AFM as 3.2 nm (Figure 2c). Similarly, the diameter of the double-stranded fibril in simulation was measured as 6.4 nm (Figure S9b), which is consistent with the diameter of 6.5 nm as observed by AFM (Figure 1d). More importantly, starting from two laterally associated single-strand protofibrils as observed in experiments (Figure 2d), the left-handed twisting tendency of the double-stranded fibril was very similar to the left-handedness found under AFM (Figure 1b) and TEM (Figure 1c). Thus, we may conclude that the all-atom simulation explained the observed fibril association very well, providing us a whole picture on the molecular level from the starting structure of **SL-3F** to single-strand protofibril, then to left-handed double-strand fibrils. The consistency of simulation and experiments gave us an opportunity to connect the molecular structure to the various fibrous behaviors.

On the basis of the aforementioned results, the exact role of the saccharide part was further identified by simulation. It appeared that two sets of hydrogen bonds were involved in the protofibrils of **SL-3F** (Scheme S4), including saccharide H-bonds that were prone to be unstructured as a result of their steric nature[29] and peptide H-bonds that having high propensity for forming β-sheet.[30,31] The quantitative comparison revealed that saccharide H-bonds were slightly more than peptide H-bonds (Figure 3g), allowing the unstructured saccharide H-bonds, to some extent, to perturb the arrangement of regular peptide H-bonds. Thus, the secondary structure of **SL-3F** protofibrils may not be as regular as a β-sheet. Expectedly, the combination of CD spectroscopy (Figure 3h), Fourier transform infrared spectrum (FT-IR), urea addition assay, and varying temperature CD assay (Figure S10) proved that triphenylalanine within **SL-3F** protofibrils indeed adopts a PP II helix conformation, which has a relatively random amide arrangement in comparison to β-sheet.[32]

A relatively random amide arrangement arising from PP II helix conformation was thought to be capable of removing certain restrictions on the spatial motion of hydrophobic phenylalanine residues,[33] allowing the moderate exposure of some hydrophobic residues on the surface of protofibrils as confirmed by the determined SASA value of 0.90 nm^2 of each middle phenylalanine residue. Meanwhile, the carboxyl groups of sialyllactose exposed on the surface of protofibrils tended to be partially deprotonated in a neutral environment, giving rise to electrostatic repulsion interactions between single-strand protofibrils. Thus, hydrophobic and electrostatic repulsion interactions appeared to be capable of antagonistically defining the association behavior of single-strand protofibrils. It was found that the double-stranding process tended to cause an increase in the negative charge on the fibril surface as confirmed by zeta-potential measurement (Figure S11a) and also give rise to a 30% decrease in the exposed area of hydrophobic residue on the fibril surface (Figure 3f). As the electrostatic repulsion force emerged as a dominant interaction for fibril association, these double-strand fibrils tended to remain highly stable rather than continue to laterally associate. We also experimentally investigated the interfibril hydrophobic interactions. The outcome showed that the process of two single-stranded protofibril associating into a double-stranded fibril is often accompanied by appreciable changes in hydrophobic interactions (Figure S11b), suggesting the involvement of hydrophobic interactions in the fibril association process.

As an intermediate species of particular interest, the ribbon-like structure involved in the association process of **SL-3F** (Figure S12a) could be rationalized on the basis of the compromise of electrostatic repulsion to hydrophobic interaction among **SL-3F** single-strand protofibrils. To further verify this point, 1 μL of NaOH solution (0.5 M) was added into the 1 mL solution of the ribbon-like structure to strengthen the electrostatic repulsion force among single-stranded protofibrils. After only 0.5 h, the ribbon-like structure already became relatively discrete, and then these discrete single-strand protofibrils further associated into ultralong double-strand fibrils within 8 h (Figure S12). The speed of fibril association in basic conditions appeared to be dozens of times faster than that in a neutral environment (Figure S13), verifying the strong contribution from electrostatic repulsion.

Taken together, it appeared that this type of glycopeptide model synergistically encoded the fibril association behavior through two key parameters. One parameter referred to the competition between the strand-forming tendency and strand-association tendency, which was encoded by the peptide moiety; another parameter is the competitive set of interactions including electrostatic repulsion and hydrophobic interaction that resided together on the surface of protofibrils, which appeared to be encoded by the saccharide moiety because the saccharide moiety not only contributed to the electrostatic repulsion but also indirectly mediated the exposure of hydrophobic residues on the surface of protofibrils

https://doi.org/10.1021/jacs.1c01951
J. Am. Chem. Soc. 2021, 143, 6622−6633

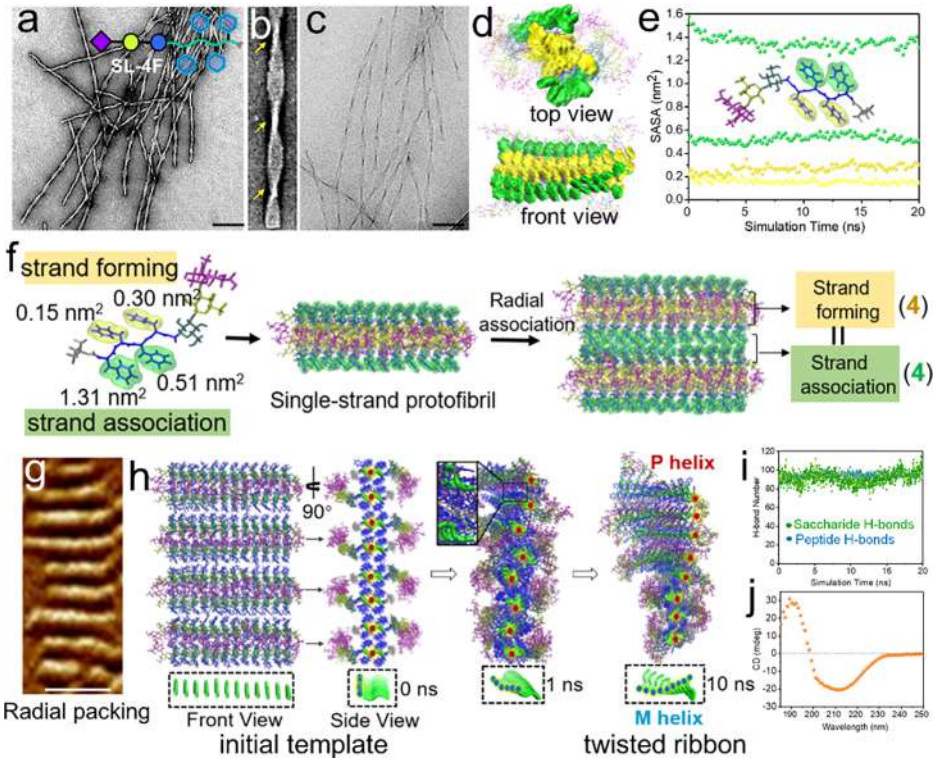

Figure 4. Fibril association behavior of **SL-4F** (1 mg/mL of **SL-4F** in water). (a, b) Negatively stained TEM (c) cryo-EM images of twisted ribbon structure of **SL-4F**, (d) top view and front view of a single-strand protofibril of **SL-4F** after blurring the saccharide moiety, (e) statistical results of the solvent-accessible surface area (SASA) of each phenylalanine residue of **SL-4F**, (f) illustration for the competition between strand-forming and strand-association, (g) the AFM height image of radially associated protofibrils of **SL-4F**, (h) relaxation process of twisted ribbon of **SL-4F** (front view and side view), (i) the statistical results of two types of H-bonds involved in protofibrils of **SL-4F**, (j) the CD result of **SL-4F** (1 mg/mL, water); scale bar in a, c, and g is 50, 50, and 10 nm, respectively.

by affecting the secondary structure of protofibrils due to their involvement in the H-bond competition with the peptide moiety.

To further unravel the contribution of the saccharide moiety on the fibril association behaviors, we selected to remove the sialic acid from sialyllactose in situ by sialidase to obtain **Lac-3F**. As shown in Figure S14c, the removal of sialic acid triggered the switch from ultralong fibrils into vesicles. The structural evolution process was traced by TEM; initially, the long fibrils collapsed into short fibrils, and then these short fibrils tended to laterally associate into bundles and further fused into nanosheets, which would spontaneously curl into vesicles in solution (Figure S14e). The decrease of aggregate size with incubation time observed in DLS assay appeared to well match this structural evolution (Figure S14f). More importantly, the conversion of secondary structure from PP II helix to β-sheet (Figure S14d) suggested that the removal of sialic acid significantly weakened the interference of unstructured saccharide H-bonds on regular peptide H-bonds; as a result, the intrinsic priority of forming a β-sheet of a peptide moiety tended to be liberated. This result appeared to exemplify the effect of the subtle trade-off of the saccharide moiety and the peptide part on the fibril association behavior.

SL-4F Radially Associates into a Twistedly Right-Handed Nanoribbon. To further determine the synergistic definition of peptides and saccharides on the fibril association behaviors, **SL-4F** (details in Scheme S6) was employed as another model to highlight the contribution from peptides via addition of one phenylalanine. By applying the same assembly scenario of **SL-3F**, it was found that **SL-4F** associated into a twisted nanoribbon structure with width centered at 25 nm and pitch of 280 nm (Figure 4a-c, S15). Excitingly, these well-defined nanoribbons were found to be right-handed (Figure 4b), indicating that **SL-4F** gave rise to a new fibril association behavior. Molecular dynamics simulation was performed again to rationalize this change. Starting from the parallel packing of **SL-4F** as **SL-3F**, the model of single-strand protofibril was built again by twisting two of the starting structures together (Figure S16a, simulation details in SI). The quantified results showed that, in the case of four hydrophobic phenylalanine residues of **SL-4F**, two (marked as yellow in Figure 4e, 4f) with SASA of 0.15and 0.30 nm^2 would contribute to strand-forming and another two (marked as green in Figure 4e,f) with SASA of 1.31 and 0.51 nm^2 would engage in strand-association (Figure 4d−f). Thus, the driving force for strand-forming (four phenylalanine residues) could be equal to that for strand-association (four phenylalanine residues) (Figure 4f); in this case, the strand-association might severely interfere the occurrence of strand-forming event.

Moreover, the involvement of two phenylalanine residues with SASA values up to 1.31 and 0.51 nm^2 into strand-association would cause a strong hydrophobic interaction among single-strand protofibrils of **SL-4F**, which would facilitate the radial association of the protofibrils while severely inhibiting their axial growth, giving rise to the radial association of short protofibrils into a ribbon structure (Figure S16b). Indeed, the AFM image showed that the **SL-4F** afforded only short protofibrils with high propensity to undergo radial association (Figure 4g, Figure S17). According to this experimental result, we defined the initial template of the

https://doi.org/10.1021/jacs.1c01951
J. Am. Chem. Soc. 2021, 143, 6622−6633

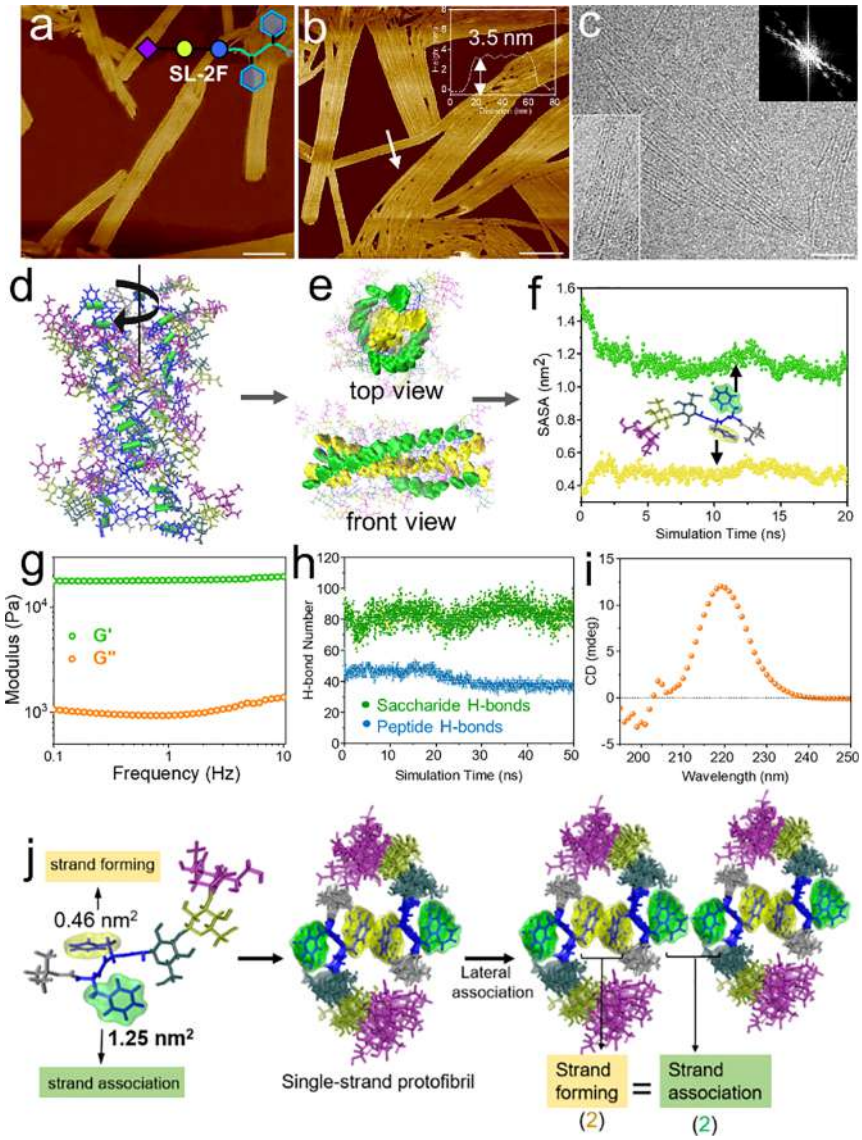

Figure 5. Fibril association behavior of **SL-2F** (1 mg/mL of **SL-2F** in water). (a, b) AFM height images, (c) Cryo-EM image of multistrand ribbon structure of **SL-2F**, (d) all-atom simulation result of a single-strand protofibril, (e) top view and front view of single-strand protofibrils of **SL-2F** after blurring the saccharide moiety, (f) the statistical results of solvent accessible surface area (SASA) of each phenylalanine residues of **SL-2F**, (g) rheological behavior of **SL-2F** gel (0.1 mass%), (h) statistical results of two types of H-bonds involved in protofibrils of **SL-2F**, (i) CD result of **SL-2F** (1 mg/mL, water), (j) illustration for the competition between strand-forming and strand-association; scale bar in a, b, and c is 100 nm.

nanoribbon (Figure 4h). After 10 ns simulation, along the left-handedness tendency that emerged in each single-strand protofibril (as marked with dotted box in Figure 4h), the entire ribbon structure yet displayed a pronounced right-handed tendency (labeled with red dot in Figure 4h, supporting movie 2). It was supposed that the molecular chirality of phenylalanine triggered the axial left-handedness of each single-strand protofibril,[34] and the twisting to the left of the single-strand protofibrils that adhered to each other via strong hydrophobic interaction may in turn drive the entire ribbon to twist to the right.[35]

Notably, in the case of **SL-4F**, the quantitative excess of peptide H-bonds to saccharide H-bonds (Figure 4i) possibly liberated the high propensity for β-sheet formation of the peptide moiety as confirmed by the CD results (Figure 4j). In general, the all-atom simulation illustrated the fibril association of **SL-4F** very well since the obtained simulation structure of the single-stranded protofibrils and twisted nanoribbons seemed to be quite consistent with the experimental results. The diameter of the single-stranded protofibril of the simulation model can be measured as 3.7 nm (Figure S17d), which was consistent with the diameter measured by AFM as 3.7 nm (Figure S17c). More importantly, starting from some radially associated single-stranded protofibrils as observed in experiments (Figure 4g), the right-handed twisting tendency of the nanoribbon was very similar to the right-handedness found under TEM (Figure 4b,c).

SL-2F Laterally Associates into Multistrand Ribbon and Hydrogel. To gain further insights to the encoding of saccharides and peptides on the fibril association, **SL-2F** was exploited as another model to emphasize the contribution from saccharide via removal of one phenylalanine. The assembly of **SL-2F** was prepared following the same procedure as for **SL-3F** and **SL-4F**. The combination of AFM and Cryo-EM results showed that **SL-2F** laterally associated into a multistrand ribbon comprising single-strand protofibrils as confirmed by a

https://doi.org/10.1021/jacs.1c01951
J. Am. Chem. Soc. 2021, 143, 6622−6633

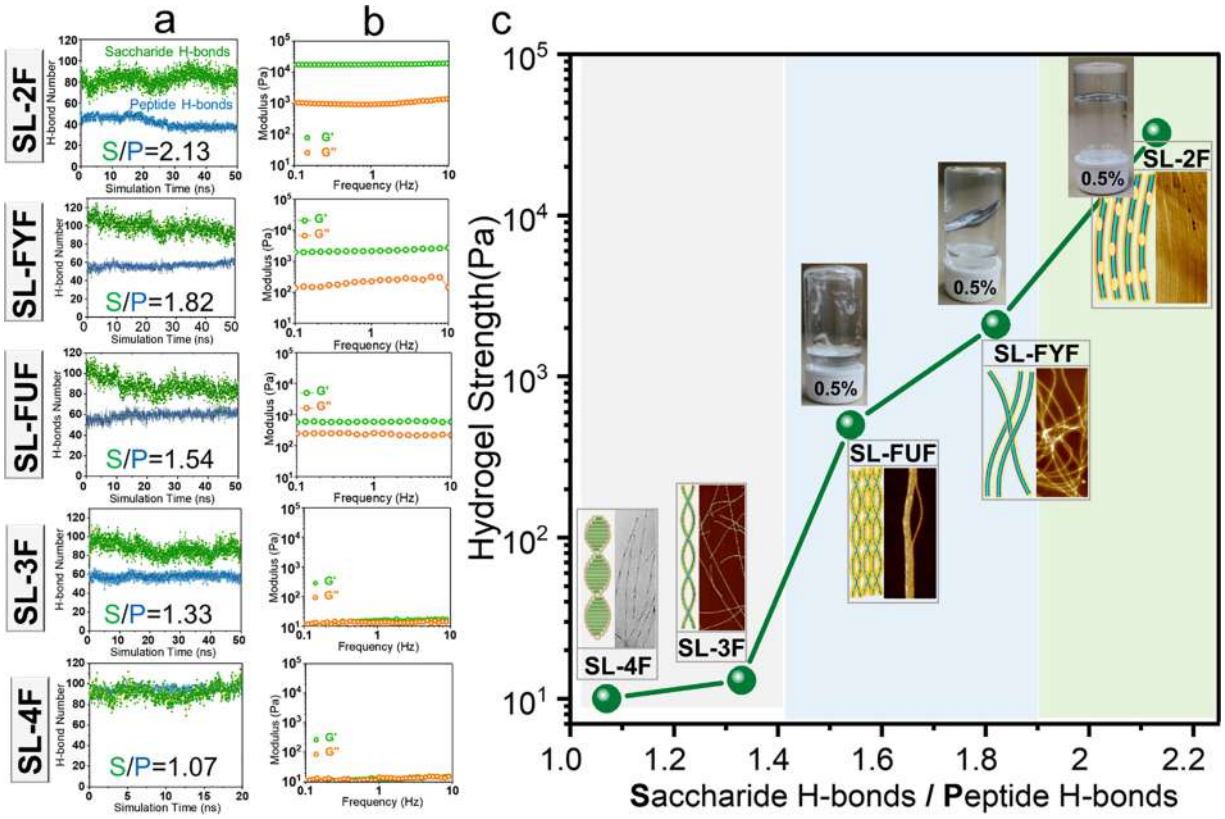

Figure 6. (a) Statistical results of two sets of H-bonds involved in protofibrils and (b) rheological behavior (0.5 mass%) of diverse glycopeptides. The saccharide H-bond/peptide H-bond (S/P) calculated from the averaged saccharide H-bonds within the simulation time was divided by the averaged peptide H-bonds within the simulation time. (c) Hydrogel strength (G') as a function of number ratios of saccharide H-bonds to peptide H-bonds (S/P).

height of about 3.5 nm (Figure 5a−c). The trace on the association process showed that in the initial 12 h **SL-2F** appeared to share a similar association process with **SL-3F**, such as micelles, protofilaments, and multistrand ribbon sequentially formed (Figure S18). Unexpectedly, after a 48 h incubation, these single-strand protofibrils tended to undergo an infinitely lateral association to afford a hydrogel with a superhigh storage modulus up to 19000 Pa, rather than associate into highly discrete double-strand fibrils like **SL-3F** (Figure 5a,g, Figure S19).

To rationalize what differentiated the fibril association behaviors of **SL-2F** and **SL-3F**, molecular dynamics simulation was performed again. The aforementioned parallel packing of **SL-2F**, like those of **SL-3F**/**SL-4F**, was employed, which was further associated into a single-strand protofibril. Then a stable single-strand protofibril structure with a pronounced left-handed tendency was yielded after 50 ns simulation (Figure 5d, Figure S20). Notably, the diameter of a stable single-strand protofibril was determined to be about 3.5 nm (Figure S20a), which was consistent to the observation from an AFM image (Figure 5b). After the saccharide moiety was blurred on the surface of a single-strand protofibril, it appeared that the exposure of hydrophobic phenylalanine residues on the surface of **SL-2F** single-strand protofibrils was more significant than that on the surface of **SL-3F** (Figure 5e, Figure 3b). The quantified results showed that the average SASA value of each phenylalanine residue exposed on the protofibril surface of **SL-2F** was 1.25 nm^2 (Figure 5f), which was nearly 40% higher than that of **SL-3F** (0.90 nm^2), implying a strong hydrophobic interaction among protofibrils of **SL-2F**. This enhanced hydrophobic interaction could be illustrated from the remodeled synergy of the saccharide part and peptide moiety. In detail, in the case of **SL-2F**, the saccharide H-bonds were twice as high as peptide H-bonds (Figure 5h), allowing the unstructured saccharide H-bonds to seriously interfere with the arrangement of regular peptide H-bonds.[36] Thus, the secondary structure adopted by diphenylalanine within **SL-2F** protofibrils may be irregular. Indeed, a prominent maximum at 220 nm arising from phenylalanine chromophores[37] indicated that diphenylalanine within **SL-2F** protofibrils adopted a random packing mode (Figure 5i). It was thought that random amide arrangement hardly imposed adequate restrictions on the spatial motion of hydrophobic phenylalanine residues, thus giving rise to a large exposure of hydrophobic residues on the surface of protofibrils.[33]

Notably, for the two phenylalanine residues of **SL-2F**, one with SASA of 0.46 nm^2 would contribute to strand-forming and another one with SASA of 1.25 nm^2 would engage in strand-association; thus, the driving force for strand-forming (two phenylalanine residues) was equal to that for strand-association (two phenylalanine residues) (Figure 5j). Similar to **SL-4F**, the strand-association might severely interfere strand-forming event, thus hardly giving rise to long fibrous structures. On the basis of the above discussion, we intend to believe that the dominant strand-association and the relatively strong hydrophobic interaction drove the single-strand protofibrils of **SL-2F** to undergo infinitely lateral association and finally to gel.

We also replaced the middle phenylalanine for strand-association of **SL-3F** with either tyrosine to obtain **SL-FYF**,

https://doi.org/10.1021/jacs.1c01951
J. Am. Chem. Soc. 2021, 143, 6622−6633

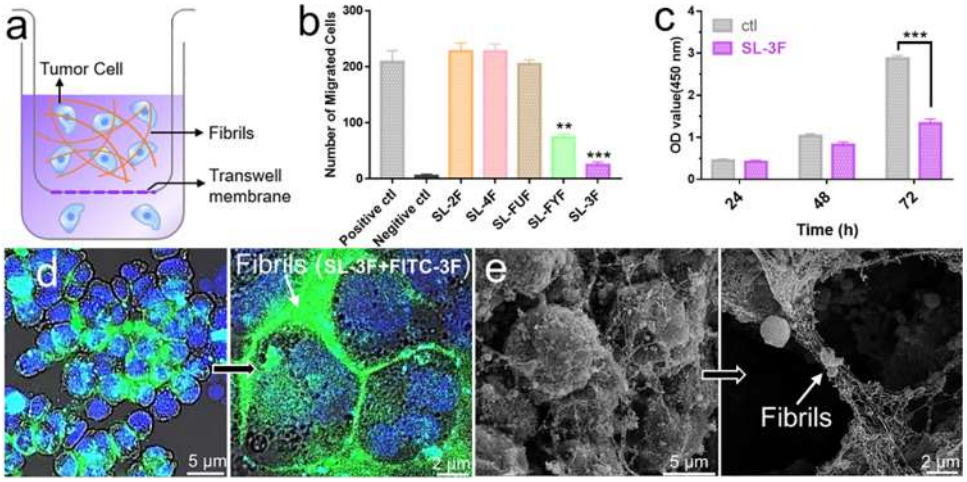

Figure 7. (a) Schematic illustration for transwell assay, (b) in vitro inhibition effect of various fibrils on B16F10 cells migration, (c) in vitro inhibition of **SL-3F** double-strand fibrils on the growth of B16F10 cells, visualization of interaction between **SL-3F** double-strand fibrils and B16F10 cells by (d) CLSM and (e) FE-SEM. Data are presented as mean ± s.e.m. Statistical significance was calculated by Student's *t* test: ***$P < 0.001$, **$P < 0.01$, *$P < 0.05$.

which may contribute to lower hydrophobic interaction than phenylalanine, or fluorophenylalanine to obtain **SL-FUF**, which could provide higher hydrophobic interaction than phenylalanine (Scheme S6). **SL-FYF** was found to associate into discrete single-strand protofibrils rather than double-strand fibers like **SL-3F**, possibly because of the weak driving force for strand-association (Figure S21a). In the case of **SL-FUF**, the most frequently occurring population appeared to be a thick fibrous structure composed of double-strand fibrils with 6.3 nm height (Figure S21j), displaying a higher tendency of lateral association than that of **SL-FYF** and **SL-3F**, which could be ascribed to the stronger driving force for strand-association.

Correlation between Molecular Building Blocks and Hydrogelation Properties. Having dissected the relationship between molecular building blocks and fibril association behaviors, next we tentatively leveraged the fibril association behaviors to bridge the molecular building blocks with some macroscopic properties in terms of hydrogelation. As mentioned above, the trade-off of saccharide H-bonds and peptide H-bonds demonstrated a critical determinant for fibril association; this inspired us to further correlate these two sets of H-bonds with hydrogelation properties of glycopeptide fibrils. We first dispersed five types of glycopeptides into water under neutral conditions with an identical concentration of 0.5 mass % and then incubated for 12 d. On the basis of the quantitative comparison of two sets of H-bonds as well as the hydrogel strength of five types of glycopeptides, an appreciable relationship between these two aspects emerged (Figure 6a,b). To better understand this relationship, we further introduced a parameter S/P, i.e., number ratio of saccharide H-bonds to peptide H-bonds to build a bridge between molecular building blocks and hydrogel strength (Figure 6c).

Fortunately, a clear relationship between the molecular building blocks and hydrogel strength can be displayed as follows. At low S/P ratios (<1.4), the dominant peptide H-bonds tended to enable the glycopeptides assembling into twisted fibrils, such as twisted double-strand fibrils of **SL-3F** and twisted nanoribbons of **SL-4F**. Notably, these twisted fibrils were found to be capable of good survival in aqueous solution and therefore always afforded solutions with no appreciable modulus, possibly since the twisted structure renders these fibrils self-limiting with respect to infinitely lateral association and bundle formation that often gives rise to hydrogel.[38,39] When the S/P ratio was increased to a higher value ($1.4 < S/P < 1.9$), more unstructured saccharide H-bonds might have interfered with the regular packing of peptide part and thus enabled larger exposure of the fluorophenylalanine residue of **SL-FUF** compared to **SL-3F**. Thus, the double-strand fibrils with a strong hydrophobic surface (as marked with light orange in Figure 6c) tended to associate into thick fibrils providing a weak hydrogel with modulus of 520 Pa. Interestingly, for **SL-FYF**, the flexible single-strand protofibrils defined by dominant unstructured saccharide H-bonds and weak driving force for strand-association afforded a hydrogel with a modulus of 2100 Pa, and the most likely reason could be the strong topological interactions among flexible single-strand protofibrils that hardly underwent any further association.[40] As the S/P ratio was more than 1.9, the fully dominant saccharide H-bonds imparted the single-strand protofibrils of **SL-2F** with very strong hydrophobic surface (as marked with orange in Figure 6c), these protofibrils tended to undergo finitely lateral association to afford a very strong hydrogel with modulus up to 32500 Pa.

The saccharide moiety, on one hand, engaged in the modulation of the hydrogelation properties with the form of saccharide H-bonds; on the other hand, the electrostatic interaction provided by the saccharide moiety could also manipulate the hydrogelation properties. For example, the addition of a small amount of HCl (1 μL, 0.5 M) would trigger the highly stable fibrils of **SL-3F** to collapse into hydrogel with a modulus of 400 Pa (Figure S22), and possibly the weakened surface negative charge gave rise to the collapse of **SL-3F** fibrils. In short, we suppose that the hydrogelation property was still governed by the saccharide moiety and peptide part.

Correlation between Fibril Association Behaviors and Antitumor Activities. Given that the fibrous populations investigated here exhibited a high structural similarity to extracellular matrices, a niche can regulate tumor invasion and migration via cell−matrix interaction.[41] Moreover, the natural tumor microenvironments often impart changes in cell−matrix interaction through variation with respect to fibril association

https://doi.org/10.1021/jacs.1c01951
J. Am. Chem. Soc. 2021, 143, 6622−6633

behavior.[42] All of these inspired us to correlate fibril association behavior with cell−matrix interactions. Thus, we selected diverse tumor cells for rationalizing this correlation on the basis of the presence of cell−matrix interactions between overexpressed sialyllactose receptors on tumor cell surfaces and sialyllactose exposed on the fibrils surface.[43]

Tumor migration assay performed by the transwell method was selected to evaluate the effect of fibril association behavior on cell−matrix interaction (Figure 7a). These five types of fibrous populations exhibited no detected cytotoxicity even when the concentration was up to 0.25 mg/mL (Figure S23). The diverse nongelling fibrous species were incubated with B16F10 cells at a concentration of 0.125 mg/mL. The in vitro outcomes showed that the double-strand fibrils of **SL-3F** and single-strand fibrils of **SL-FYF** could display certain inhibition on the migration of B16F10 cells while double-strand fibrils of **SL-3F** exhibited the most effective inhibition, but the fibrous species of **SL-2F**, **SL-4F**, or **SL-FUF** could not (Figure 7b, Figure S24). The universality of the double-strand fibrils of **SL-3F** to inhibit migration of diverse tumor cells such as BV-2 and HepG 2 is also demonstrated in the Supporting Information (Figure S25). We also tentatively quantified interactions between **SL-3F** fibrils and B16F10 cells, and the outcome showed that each microgram fibrils of **SL-3F** could adhere (2.8 ± 0.5) × 10^3 B16F10 cells (Figure S26).

The double-strand fibrils of **SL-3F** were also proven to be capable of delaying the growth of tumor cells (Figure 7c). To further rationalize the mechanism underlying inhibition of tumor cell migration and growth, the visualization of the interaction between distinct fibrils and tumor cells was performed. Co-assembly of **SL-3F** or **SL-FYF** with **FITC-3F** afforded the corresponding fluorescence-labeled fibrils, which were named as **SL-3F+FITC-3F** and **SL-FYF+FITC-3F**, respectively. When these fluorescence-labeled fibrils were cocultured with B16F10 cells for 48 h, **SL-3F+FITC-3F** appeared to tightly stick to the surface of B16F10 cells like molecular glue[44] (Figure 7d), whereas neither **SL-FYF+FITC-3F** nor only **FITC-3F** could effectively stick to the surface of B16F10 cells (Figure S27), suggesting that the capability of sticking cells together of the **SL-3F** fibrils might be one of the factors that can inhibit tumor migration. The FE-SEM images provided high resolution evidence of interaction between double-strand fibrils and tumor cells (Figure 7e).

The correlation between fibril association behaviors and antitumor activities was further interrogated by in vivo assay. **SL-FYF** and **SL-3F**, two fibrous species with similar morphology of high aspect ratio but distinct association behavior (the former is single-stranded, the latter is double-stranded), was selected to perform the in vivo assay. We first injected B16F10 cells into the abdominal cavity of the mice and then injected the fibrous species of **SL-FYF** and **SL-3F** at the same location of the tumor. After 6 d incubation, the antitumor activities of **SL-3F** seemed to outperform that of **SL-FYF** (Figure S28), which was well consistent with the in vitro results (Figure 7b). This difference in antitumor activity seemly emerged from the distinct capabilities of sticking tumor cells of fibrous species, which was significantly influenced by their fibril association behaviors.

■ CONCLUSION

In summary, we have experimentally and theoretically demonstrated the synergistic encoding of saccharides and peptides on fibril association behaviors based on a designed set of glycopeptide models. The subtle trade-off of oligosaccharide and oligopeptide components was proven to be a determinant that regulates the growth direction as well as chirality of fibrils. The fibril association was also identified as a useful tool to bridge the molecular building blocks and some macroscopic properties in terms of hydrogelation as well as antitumor activities. Notably, the double-strand fibrils of **SL-3F** with a super high aspect ratio up to 10^5 were found to be capable of highly surviving in solution and firmly sticking on the tumor cells surface. Glycosylation is a ubiquitous phenomenon in Nature, which is involved in various fibrous association processes with distinct effects. We hope that the molecular details of saccharides on fibrous association may reveal some mechanisms involved by glycans and predict unraveled disciplines. In short, the reported comprehensive landscape of fibril association behaviors may provide tools to decode naturally occurring fibril association and shed unique insight on fibrous material design.

■ ASSOCIATED CONTENT

Supporting Information

The Supporting Information is available free of charge at https://pubs.acs.org/doi/10.1021/jacs.1c01951.

Synthesis, prescreening of glycopeptide modes, characterization of fibrils, and antitumor activities of the fibrils (PDF)

Stable double-strand fibril structure with striking left-handed tendency (MPG)

Nanoribbon with pronounced right-handed tendency (MPG)

■ AUTHOR INFORMATION

Corresponding Author

Guosong Chen − *The State Key Laboratory of Molecular Engineering of Polymers and Department of Macromolecular Science and Multiscale Research Institute of Complex Systems, Fudan University, Shanghai 200433, P.R. China;* orcid.org/0000-0001-7089-911X; Email: guosong@fudan.edu.cn

Authors

Rongying Liu − *The State Key Laboratory of Molecular Engineering of Polymers and Department of Macromolecular Science, Fudan University, Shanghai 200433, P.R. China*

Ran Zhang − *State Key Laboratory of Polymer Physics and Chemistry, Changchun Institute of Applied Chemistry, Chinese Academy of Sciences, Changchun 130022, P.R. China*

Long Li − *The State Key Laboratory of Molecular Engineering of Polymers and Department of Macromolecular Science, Fudan University, Shanghai 200433, P.R. China*

Zdravko Kochovski − *Department for Electrochemical Energy Storage, Helmholtz-Zentrum Berlin für Materialien und Energie, 14109 Berlin, Germany*

Lintong Yao − *The State Key Laboratory of Molecular Engineering of Polymers and Department of Macromolecular Science, Fudan University, Shanghai 200433, P.R. China*

Mu-Ping Nieh − *Polymer Program, Institute of Materials Science and Department of Chemical and Biomolecular Engineering, University of Connecticut, Storrs, Connecticut 06269, United States;* orcid.org/0000-0003-4462-8716

https://doi.org/10.1021/jacs.1c01951
J. Am. Chem. Soc. 2021, 143, 6622−6633

Yan Lu − *Department for Electrochemical Energy Storage, Helmholtz-Zentrum Berlin für Materialien und Energie, 14109 Berlin, Germany; Institute of Chemistry, University of Potsdam, 14476 Potsdam, Germany;* orcid.org/0000-0003-3055-0073

Tongfei Shi − *State Key Laboratory of Polymer Physics and Chemistry, Changchun Institute of Applied Chemistry, Chinese Academy of Sciences, Changchun 130022, P.R. China;* orcid.org/0000-0002-6763-2200

Complete contact information is available at: https://pubs.acs.org/10.1021/jacs.1c01951

Notes

The authors declare no competing financial interest.

■ ACKNOWLEDGMENTS

G.C. thanks NSFC/China (Nos. 51721002, 21861132012, 91956127, 21975047) for financial support. R.Z. thanks NSFC/China (No. 21674114, 91956127) for financial support. Y.L. thanks the Deutsche Forschungsgemeinschaft (DFG, German Research Foundation)—Project No. 410871749 for financial support. The authors thank the Joint Lab for Structural Research at the Integrative Research Institute for the Sciences (IRIS Adlershof, Berlin) for Cryo-EM imaging. This work is supported by the Shanghai Municipal Science and Technology Major Project (No.2018SHZDZX01) and ZJ Lab.

■ REFERENCES

(1) Lieleg, O.; Claessens, M. M.; Bausch, A. R. Structure and dynamics of cross-linked actin networks. *Soft Matter* **2010**, *6*, 218−225.

(2) Marino, M.; Vairo, G. Multiscale Elastic Models of Collagen Biostructures: From Cross-Linked Molecules to Soft Tissues. *Multiscale Computer Modeling in Biomechanics and Biomedical Engineering* **2013**, *14*, 73.

(3) Lim, C. Z. J.; et al. Subtyping of circulating exosome-bound amyloid β reflects brain plaque deposition. *Nat. Commun.* **2019**, *10*, 1.

(4) Baker, M. B.; Albertazzi, L.; Voets, I. K.; Leenders, C. M. A.; Palmans, A. R. A.; Pavan, G. M.; Meijer, E. W. Consequences of chirality on the dynamics of a water-soluble supramolecular polymer. *Nat. Commun.* **2015**, *6*, 6234.

(5) Yano, K.; Hanebuchi, T.; Zhang, X. J.; Itoh, Y.; Uchida, Y.; Sato, T.; Matsuura, K.; Kagawa, F.; Araoka, F.; Aida, T. Supramolecular Polymerization in Liquid Crystalline Media: Toward Modular Synthesis of Multifunctional Core - Shell Columnar Liquid Crystals. *J. Am. Chem. Soc.* **2019**, *141*, 10033−10038.

(6) Weyandt, E.; ter Huurne, G. M.; Vantomme, G.; Markvoort, A. J.; Palmans, A. R. A.; Meijer, E. W. Photodynamic Control of the Chain Length in Supramolecular Polymers: Switching an Intercalator into a Chain Capper. *J. Am. Chem. Soc.* **2020**, *142*, 6295−6303.

(7) Bera, S.; Mondal, S.; Xue, B.; Shimon, L. J. W.; Cao, Y.; Gazit, E. Rigid helical-like assemblies from a self-aggregating tripeptide. *Nat. Mater.* **2019**, *18*, 503−509.

(8) Bera, S.; Xue, B.; Rehak, P.; Jacoby, G.; Ji, W.; Shimon, L. J. W.; Beck, R.; Kral, P.; Cao, Y.; Gazit, E. Self-Assembly of Aromatic Amino Acid Enantiomers into Supramolecular Materials of High Rigidity. *ACS Nano* **2020**, *14*, 1694−1706.

(9) Hendrikse, S. I. S.; Su, L.; Hogervorst, T. P.; Lafleur, R. P. M.; Lou, X. W.; Marel, G. A. V. D.; Codee, J. D. C.; Meijer, E. W. Elucidating the Ordering in Self-Assembled Glycocalyx Mimicking Supramolecular Copolymers in Water. *J. Am. Chem. Soc.* **2019**, *141*, 13877−13886.

(10) Adamcik, J.; et al. Understanding amyloid aggregation by statistical analysis of atomic force microscopy images. *Nat. Nanotechnol.* **2010**, *5*, 423−428.

(11) Freeman, R.; et al. Reversible self-assembly of superstructured networks. *Science* **2018**, *362*, 808−813.

(12) Jones, C. D.; Simmons, H. T. D.; Horner, K. E.; Liu, K.; Thompson, R. L.; Steed, J. W. Braiding, branching and chiral amplification of nanofibres in supramolecular gels. *Nat. Chem.* **2019**, *11*, 375−381.

(13) Khurana, R.; Ionescu-Zanetti, C.; Pope, M.; Li, J.; Nielson, L.; Ramirez-Alvarado, M.; Regan, L.; Fink, A. L.; Carter, S. A. A general model for amyloid fbril assembly based on morphological studies using atomic force microscopy. *Biophys. J.* **2003**, *85*, 1135−1144.

(14) Ridgley, D. M.; Barone, J. R. Evolution of the amyloid fiber over multiple length scales. *ACS Nano* **2013**, *7*, 1006−1015.

(15) Hennet, T. Collagen glycosylation. *Curr. Opin. Struct. Biol.* **2019**, *56*, 131−13.

(16) Lewis, Y. E.; Galesic, A.; Levine, P. M.; De Leon, C. A.; Lamiri, N.; Brennan, C. K.; Pratt, M. R. O-GlcNAcylation of α-synuclein at serine 87 reduces aggregation without affecting membrane binding. *ACS Chem. Biol.* **2017**, *12*, 1020−1027.

(17) Signas, C.; et al. Nucleotide sequence of the gene for a fibronectin-bindng protein from Staphylococcus aureus: use of this peptide seuence in the synthesis of biologically active peptides. *Proc. Natl. Acad. Sci. U. S. A.* **1989**, *86*, 699−703.

(18) Marotta, N. P.; Lin, Y. H.; Lewis, Y. E.; Ambroso, M. R.; Zaro, B. W.; Roth, M. T.; Pratt, M. R. O-GlcNAc modification blocks the aggregation and toxicity of the protein α-synuclein associated with Parkinson's disease. *Nat. Chem.* **2015**, *7*, 913−920.

(19) Levine, P. M.; Galesic, A.; Balana, A. T.; Mahul-Mellier, A. L.; Navarro, M. X.; De Leon, C. A.; Pratt, M. R. α-Synuclein O-GlcNAcylation alters aggregation and toxicity, revealing certain residues as potential inhibitors of Parkinson's disease. *Proc. Natl. Acad. Sci. U. S. A.* **2019**, *116*, 1511−1519.

(20) Galesic, A.; Rakshit, A.; Cutolo, G.; Pacheco, R. P.; Balana, A. T.; Moon, S. P.; Pratt, M. R. Comparison of N-Acetyl-Glucosamine to Other Monosaccharides Reveals Structural Differences for the Inhibition of α-Synuclein Aggregation. *ACS Chem. Biol.* **2021**, *16*, 14−19.

(21) Reches, M.; Gazit, E. Casting metal nanowires within discrete self-assembled peptide nanotubes. *Science* **2003**, *300*, 625−627.

(22) Brown, N.; Lei, J.; Zhan, C.; Shimon, L. J. W.; Adler-Abramovich, L.; Wei, G.; Gazit, E. Structural polymorphism in a self-assembled tri-aromatic peptide system. *ACS Nano* **2018**, *12*, 3253−3262.

(23) Fleming, S.; Ulijn, R. V. Design of nanostructures based on aromatic peptide amphiphiles. *Chem. Soc. Rev.* **2014**, *43*, 8150−8177.

(24) Pappas, C. G.; et al. Dynamic peptide libraries for the discovery of supramolecular nanomaterials. *Nat. Nanotechnol.* **2016**, *11*, 960−967.

(25) Iconomidou, V. A.; Hamodrakas, S. J. Natural protective amyloids. *Curr. Protein Pept. Sci.* **2008**, *9*, 291−309.

(26) Gelenter, M. D.; et al. The peptide hormone glucagon forms amyloid fibrils with two coexisting β-strand conformations. *Nat. Struct. Mol. Biol.* **2019**, *26*, 592−598.

(27) Maji, S. K.; Drew, M. G.; Banerjee, A. First crystallographic signature of amyloid-like fibril forming β-sheet assemblage from a tripeptide with non-coded amino acids. *Chem. Commun.* **2001**, 1946−1947.

(28) Kemper, B.; Zengerling, L.; Spitzer, D.; Otter, R.; Bauer, T.; Besenius, P. Kinetically controlled stepwise self-assembly of AuI-metallopeptides in water. *J. Am. Chem. Soc.* **2018**, *140*, 534−537.

(29) van de Bovenkamp, F. S.; Hafkenscheid, L.; Rispens, T.; Rombouts, Y. The emerging importance of IgG Fab glycosylation in immunity. *J. Immunol.* **2016**, *196*, 1435−1441.

(30) Ma, X.; Wang, Y. Q.; Hua, J. A.; Xu, C. Y.; Yang, T.; Yuan, J.; Chen, G. Q.; Guo, Z. J.; Wang, X. Y. A β-sheet-targeted theranostic agent for diagnosing and preventing aggregation of pathogenic peptides in Alzheimer's disease. *Sci. China: Chem.* **2020**, *63*, 73−82.

(31) Yin, Q.; Liu, J. J.; Tian, M. T.; Xie, H.; Shen, L.; Sun, T. L. Protein Fibrillation in Neurodegenerative Diseases and Its Chiral Interaction with Interfaces. *Acta Polym. Sin.* **2019**, *50*, 575−587.

(32) Bochicchio, B.; Tamburro, A. M. Polyproline II structure in proteins: identification by chiroptical spectroscopies, stability, and functions. *Chirality* **2002**, *14*, 782−792.
(33) Ortony, J. H.; Newcomb, C. J.; Matson, J. B.; Palmer, L. C.; Doan, P. E.; Hoffman, B. M.; Stupp, S. I. Internal dynamics of a supramolecular nanofibre. *Nat. Mater.* **2014**, *13*, 812−816.
(34) Yue, B. B.; Zhu, L. L. Dynamic modulation of supramolecular chirality driven by factors from internal to external level. *Chem. - Asian J.* **2019**, *14*, 2172−2180.
(35) Efrati, E.; Irvine, W. T. M. Orientation-dependent handedness and chiral design. *Phys. Rev. X* **2014**, *4*, 011003.
(36) Schoenmakers, S. M. C.; Leenders, C. M. A.; Lafleur, R. P. M.; Lou, X. W.; Meijer, E. W.; Pavan, G. M.; Palmans, A. R. A. Impact of the water-compatible periphery on the dynamic and structural properties of benzene-1,3,5-tricarboxamide based amphiphiles. *Chem. Commun.* **2018**, *54*, 11128−11131.
(37) Hamley, I. W.; Krysmann, M. J.; Kelarakis, A.; Castelletto, V.; Noirez, L.; Hule, R. A.; Pochan, D. J. Nematic and columnar ordering of a PEG-peptide conjugate in aqueous solution. *Chem. - Eur. J.* **2008**, *14*, 11369−11375.
(38) Marty, R.; Nigon, R.; Leite, D.; Frauenrath, H. Two-Fold odd - even effect in self-assembled nanowires from oligopeptide-polymer-substituted perylene bisimides. *J. Am. Chem. Soc.* **2014**, *136*, 3919−3927.
(39) Cui, C. Y.; Chen, X. Y.; Liu, B.; Wu, T. L.; Fan, C. C.; Liu, W. G. A High Strength Instant Adhesive Nano-hybrid Hydrogel as First-aid Bandage. *Acta Polym. Sin.* **2019**, *50*, 613−622.
(40) Raghavan, S. R.; Douglas, J. F. The conundrum of gel formation by molecular nanofibers, wormlike micelles, and filamentous proteins: gelation without cross-links? *Soft Matter* **2012**, *8*, 8539−8546.
(41) Theocharis, A. D.; Skandalis, S. S.; Gialeli, C.; Karamanos, N. K. Extracellular matrix structure. *Adv. Drug Delivery Rev.* **2016**, *97*, 4−27.
(42) Walters, N. J.; Gentleman, E. Evolving insights in cell-matrix interactions: Elucidating how non-soluble properties of the extracellular niche direct stem cell fate. *Acta Biomater.* **2015**, *11*, 3−16.
(43) Chung, T. W.; et al. Sialyllactose suppresses angiogenesis by inhibiting VEGFR-2 activation, and tumor progression. *ONCOTARGET* **2017**, *35*, 58152−58162.
(44) Mogaki, R.; Okuro, K.; Aida, T. Molecular glues for manipulating enzymes: trypsin inhibition by benzamidine-conjugated molecular glues. *Chem. Sci.* **2015**, *6*, 2802−2805.

https://doi.org/10.1021/jacs.1c01951
J. Am. Chem. Soc. 2021, 143, 6622−6633